

Study of Processing Map and Effect of Hot Rolling on Mechanical Properties of Aluminum 5083 Alloy

Amitava Rudra^{1,2} · Mohammad Ashiq^{1,2} · Jitendar Kumar Tiwari^{1,2} · Satyabrata Das³ · Rupa Dasgupta³

Received: 24 February 2020 / Accepted: 15 May 2020 / Published online: 28 May 2020
© The Indian Institute of Metals - IIM 2020

Abstract Hot deformation behavior of aluminum 5083 alloy was studied based on the compression test done up to true strain 0.5 in the temperature range of 473–773 K and strain rate range of 0.01–10 s⁻¹. The Arrhenius equations were used to evaluate the average activation energy for deformation. Processing map was developed to identify the optimum, safe and unsafe zones for processing based on the compression data. Electron backscattered diffraction (EBSD) and scanning electron microscopy images revealed the underlying micro-mechanisms at various deformation conditions. Varying fraction of dynamic recrystallization was found to coexist with dynamic recovery at high deformation temperature and different strain rates. Based on the safe deformation zone, hot rolling was attempted and up to 80% reduction of initial thickness was achieved. EBSD analysis showed that the percentage of dynamically recrystallized grains increased with increment in rolling reduction. Progressive and substantial increment in yield strength, ultimate tensile strength, ductility and bulk hardness was achieved with increment in rolling reductions.

Keywords Hot deformation · Aluminum · Activation energy · Processing map · Rolling · Mechanical property

1 Introduction

Aluminum 5083 is a strain-hardened alloy of aluminum 5xxx wrought alloy series with Mg and Mn being the main alloying elements, respectively. It is a solid solution strengthened alloy with medium strength, excellent resistance to corrosion in saline water as well as the industrial chemical environment, good formability and weldability. It is commercially available in various strain hardening states including H111, H123, H321, etc. This alloy has been extensively used in marine environments, automobiles, chemical industries, etc. [1–3]. Till now investigations related to cold deformation at room temperature and cryogenic temperature with subsequent annealing [4–7], hot deformation (tension, torsion, compression) with constitutive analysis [8–10], hot extrusion [11], hot rolling with numerical analysis [12, 13] and recrystallization kinetics after hot rolling [14] for this alloy have been done. These works explore the evaluation of activation energy, microstructure development under various deformation conditions, microstructural changes during and after extrusion, rolling for this alloy. Unfortunately, a systematic study related to optimization of hot deformation behavior and further study or application of the same have not been explored for this alloy till now.

The optimization of high temperature flow behavior by processing map [15] based on dynamic material model (DMM) [16] has been a fascinating choice for the researchers as it provides a deep insight into processing a material at industrial conditions. It suggests a processing window which involves desirable process phenomena such as dynamic recovery (DRV), dynamic recrystallization (DRX) and a list of undesirable phenomena under a vast processing range. Several studies related to various Al and other alloys, composites have been done successfully by

✉ Amitava Rudra
rudraamitava499@gmail.com

¹ Academy of Scientific and Innovative Research (AcSIR), Bhopal 462026, India

² CSIR-Advanced Materials and Processes Research Institute, Bhopal 462026, India

³ Ex-CSIR-Advanced Materials and Processes Research Institute, Bhopal 462026, India

this processing map [17–24]. Microstructural studies at various processing zones by suitable characterization techniques established the understanding of micro-mechanisms of hot deformation for these materials.

In the present work, the high-temperature isothermal compression test at different temperatures and strain rates was performed to determine the hot flow stress of Al-5083 alloy. The flow behavior was used to investigate intrinsic workability of the alloy by developing processing map with supportive microstructural study through electron backscattered diffraction (EBSD) and scanning electron microscopy (SEM). After identification of optimized, safe and unsafe zones for processing, multipass rolling was attempted in the secure zone of processing as described as arrived at through processing map. It was followed by microstructural and mechanical property evaluation to witness the effect of hot rolling.

2 Material and Experimental Details

The present Al-5083 alloy was fabricated by liquid metallurgy method. The alloy was cast in finger-shaped molds of 20 mm diameter and cylindrical billet of 85 mm diameter. As-cast sample of suitable size was cut from the finger, metallographically polished and etched to see the initial microstructure. The cast materials were homogenized at 793 K for 12 h to increase the workability. For compression test, specimens with a height of 15 mm and a diameter of 10 mm were machined according to ASTM E209. The compression test was performed at a universal tensile testing machine (INSTRON 8801) with insulating chamber and resistance furnace heating attachment. The friction was minimized between sample and crosshead by applying graphite powder at the surface of the former. All the samples were compressed in the temperature range of 473–773 K with an interval of 100 K and under the strain rates of 0.01, 0.1, 1 and 10 s^{-1} . Once the samples reached a specified temperature, they were soaked for 5 min to obtain temperature homogeneity. Subsequently, samples were compressed up to a true strain of 0.5 followed by immediate water quenching to preserve the deformed microstructure. The compression flow curves were recorded in computer. The heating rate was controlled, and the corresponding specimen temperature was measured by using a K-type thermocouple. During the compression test at high strain rate (10 s^{-1}), no flow softening due to the adiabatic heating was observed. As aluminum alloys possess high thermal conductivity, the flow behavior does not affect much due to deformation-induced heating at a strain rate of 10 s^{-1} as seen in previous studies [25, 26]. Barrelling effect was also very low as friction was minimized by suitable lubrication technique. The hot compressed

samples were cut through midway along their longitudinal axis, and the area around the midpoint was selected for microstructural study. For rolling at high temperature, circular plates of 75 mm diameter and 10 mm thickness were machined from cylindrical billets perpendicular to its longitudinal direction. This ensured nearly homogeneous composition throughout the plates. These plates were further faced for 1 mm each side to get flat surfaces. The homogenized plates were reheated at 793 K for 30 min prior to hot rolling. The plates underwent different amounts of desired reductions (20%–80% of initial thickness) at two high-end rolling mills with attachment of induction furnace to heat the rollers. The rollers were maintained at a temperature 623 K throughout the rolling process. Specimens that were reduced by more than 30% underwent intermediate annealing for 5 min. The plates were water quenched once the desired reduction was achieved. The tensile test specimens were cut from the rolled plates according to ASTM B557 with the help of wire cut EDM and tested at room temperature through INSTRON 8801 UTM machine with a strain rate of 0.001 s^{-1} . The test was performed at least three times for each type of specimens to ensure reliability. The bulk hardness test was carried out at a Brinell hardness testing machine (Model: KB 250 BVRZ). A 62.5 kgf load for 10 s was applied on mirror polished sample surface by a steel ball of 10 mm diameter. The indentations were observed by optical microscope attached with the indenter. At least six indentations were taken, and their average value was considered as final hardness.

The chemical composition of the alloy was evaluated by optical emission spectrometer. Field emission scanning electron microscope (Nova Nano SEM 430, FEI) attached with energy-dispersive X-ray spectroscopy was used to see the microstructures of samples under various conditions. The TCL OIM, EDAX software was used for EBSD data acquisition and analysis along with HIKARI Super (EDAX) EBSD detector. The accelerating voltage was 20 kV and the emission current was 116 μA during EBSD scan. The measurements were done in the hexagonal grid. The step size, binning and area of study were 0.6 μm , 6×6 and $600\text{ }\mu\text{m} \times 600\text{ }\mu\text{m}$, respectively. The confidence index (CI) cutoff was taken as 0.2 to increase the reliability of EBSD data. Misorientation angle below 2° was ignored for each specimen to remove angular resolution error. The image quality (IQ) map, inverse pole figure (IPF) map, grain boundary misorientation distribution, grain size distribution for the selected region ($600\text{ }\mu\text{m} \times 600\text{ }\mu\text{m}$) were determined using EBSD postprocessing software (TSL-OIM, EDAX). For FESEM studies, samples were metallographically polished and etched in freshly prepared Keller's reagent. For EBSD experiment, samples were polished with noncrystalline colloidal silica of particle size 0.03 μm after conventional metallographic

polishing. This was followed by electro-polishing at room temperature in an electrolyte of 20:80 volumetric ratios of methanol and perchloric acid for 15 s at 12 V.

3 Results and Discussion

3.1 Chemical Composition and Initial Microstructure

The average chemical compositions of the alloy as obtained from the test are presented in Table 1. The density of the alloy is measured as 2.648 g/cc by Archimedes principle. Figure 1a reveals the initial dendritic microstructure of alloy in the as cast-condition. It can be seen that intermetallic particles are precipitated at the grain boundary and they are not uniformly distributed. Various kinds of intermetallic particles of Al–Mg (almost the same color as of Al matrix), Al–Mg–Si (gray with bright surrounding), Al–Mg–Mn–Fe (bright colored) have been characterized by EDX spectrum as shown in Fig. 1b, c. The presence of similar kinds of intermetallics was reported by previous researchers [27, 28]. Figure 1d shows the EBSD microstructure of alloy in homogenized condition. It can be observed that the grains are randomly oriented and the average misorientation angle is measured between 30° and 60°. The average grain size is measured as 180 μm approximately.

3.2 Flow Stress Behavior

The true stress–strain graphs of the present alloy under different deformation conditions are shown in Fig. 2a–d. It can be clearly seen that initially the flow stress increases rapidly and with an increment in strain, the rate of increment in flow stress decreases. Eventually, the flow stress reaches a maximum value before it saturates with the increment in strain up to the final value. At the primary stage, generation and subsequent entanglement of dislocations known as strain hardening occur at a very fast rate. This causes the steady increment in stress with strain. As the number of dislocations in the material approaches a critical value, the probability of dislocation annihilation and rearrangement to a lower energy configuration increases; thus, thermal activation (dynamic softening) processes start. This activation process counteracts the

strain hardening rate and causes the decrement in the latter. After this, a certain stage is reached where the competition between dislocation generation and dislocation annihilation and rearrangement due to dynamic softening reaches an equilibrium state. Due to the persistence of this dynamic balance, flow stress remains almost constant [29].

At a particular strain rate, the attainment of steady-state flow stress extends with a decrement in deformation temperature. At the lowest experimental temperature (473 K) and the highest experimental strain rate (10 s⁻¹) condition, though the rate of increment in flow stress decreases, it is unable to achieve a saturation value up to the final strain. At higher temperatures (0.8–0.9T_m, T_m = melting temperature in Kelvin), the dislocation cross-slip, glide and climb phenomena occur at a very high rate. This ensures softening processes such as dynamic recovery (DRV) and dynamic recrystallization (DRX) occur readily and counteract strain hardening. At lower temperatures, thermal activation processes are not very effective to slow down strain hardening rate due to lower dislocation mobility. It is also observed that at a particular strain rate, the peak stress decreases with increment in temperature. It is due to the amplification of thermal softening processes at elevated temperatures. However, at a given temperature, the flow stress shows a reverse behavior with increment in strain rate due to the occurrence of dislocation generation and multiplication at a higher rate [30, 31].

The change in dislocation density (ρ) with deformation strain (ε) can be correlated with work hardening and dynamic softening (recovery) with the help of the following equation [32];

$$\frac{d\rho}{d\varepsilon} = U - \Omega\rho \tag{1}$$

where U is a multiplication term and represents work hardening, Ω is dynamic softening coefficient and is a function of temperature and strain rate.

When steady-state condition is reached after work hardening, the change in dislocation density with respect to strain becomes zero, i.e. $\frac{d\rho}{d\varepsilon} = 0$. Therefore, Eq. (1) can be written as,

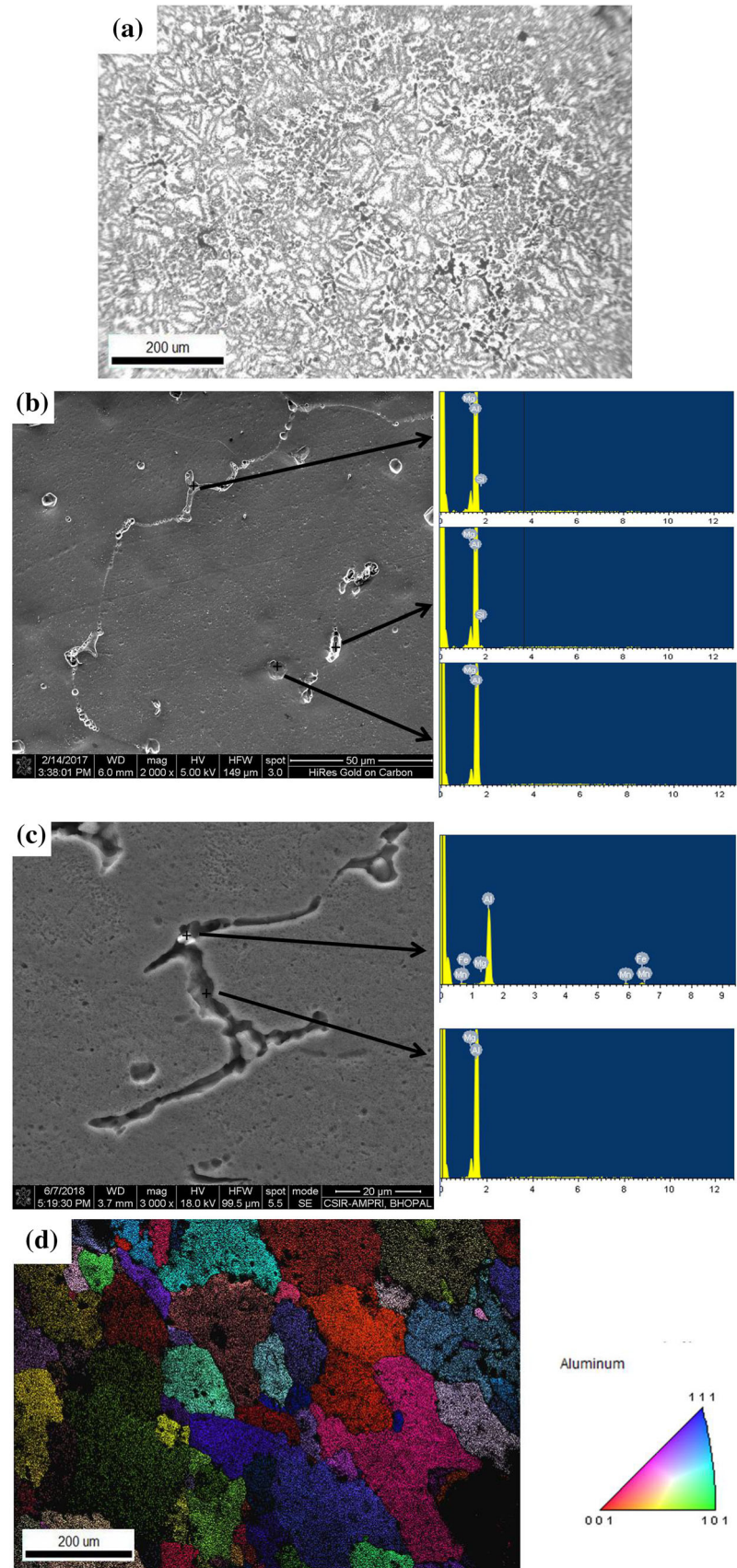
$$\rho = \frac{U}{\Omega} \tag{2}$$

Now, the flow stress (σ) is related to dislocation density (ρ) by the equation [33],

Table 1 Chemical compositions of current Al-5083 alloy in wt%

Mg	Mn	Cr	Fe	Si	Zn	Ti	Al
4.43%	0.653%	0.14%	0.18%	0.32%	0.09%	0.008%	Balanced

Fig. 1 **a** Optical microstructure of alloy in as-cast condition, **b**, **c** EDX spectrum showing different kinds of intermetallic compounds, **d** Inverse pole figure map of alloy after homogenization



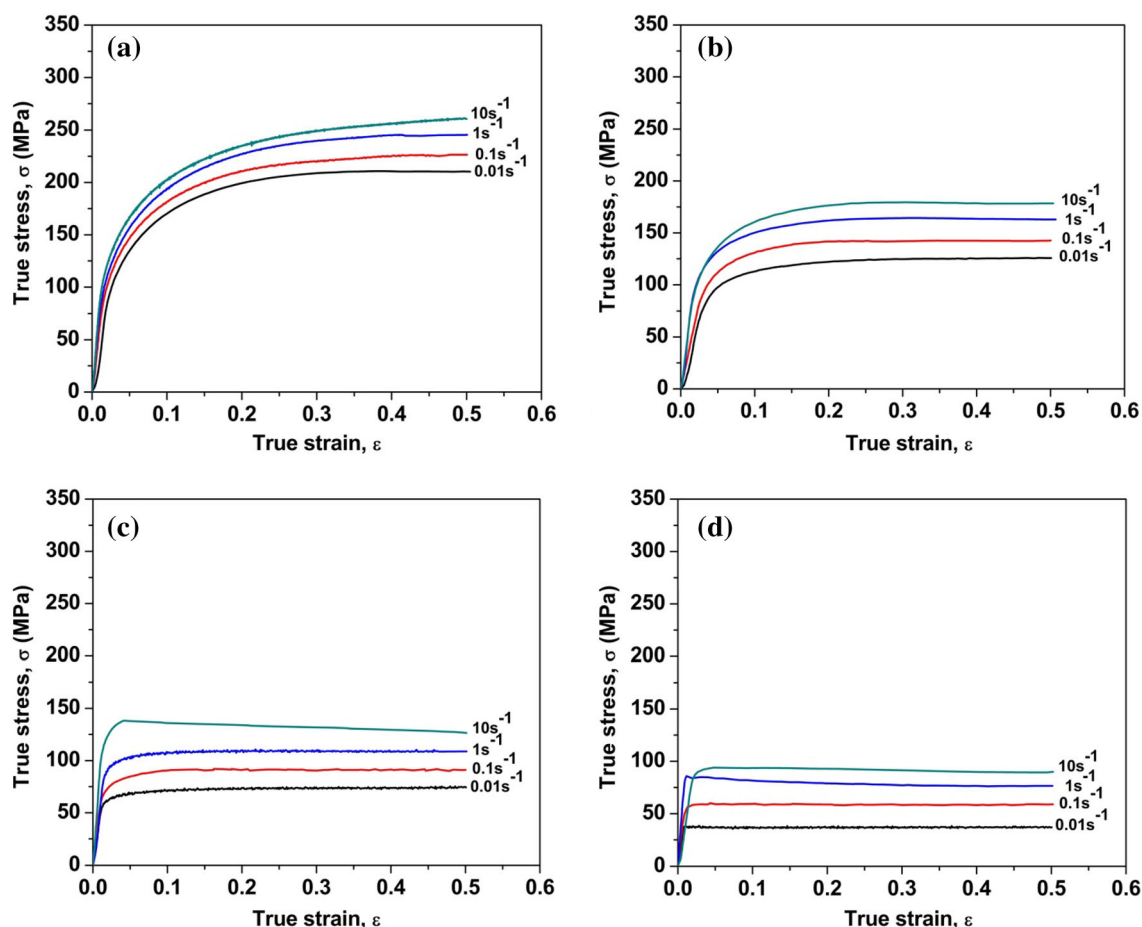


Fig. 2 True stress–strain curves of aluminum 5083 alloy at a strain rate range of 0.01–10 s⁻¹ and at temperature of **a** 473 K, **b** 573 K, **c** 673 K, **d** 773 K

$$\sigma = \alpha Gb\sqrt{\rho} \tag{3}$$

where α is material constant, G is shear modulus of material and b is the Burgers vector of dislocation.

Substituting Eq. (2) into Eq. (3), we get steady-state flow stress

$$\sigma_s = \alpha Gb\sqrt{\frac{U}{\Omega}} \tag{4}$$

Therefore, it can be said that the steady-state flow value is proportional to the square root of work hardening and inversely proportional to the square root of dynamic softening. Now, at a constant temperature, the multiplication rate of dislocations or entanglement sharply increases with increment in strain rate. However, the thermal activation rate changes very little due to the same thermal energy given to the dislocations. Thus, the flow stress reaches a higher value before attainment of steady-state condition. Inversely, at a particular strain rate, the dislocation multiplicity rate or work hardening rate remains constant, whereas dislocation mobility largely

increases with increment in temperature. Therefore, dynamic softening rate prevails over work hardening very easily. This factor does not allow the flow stress to go up to a high value, and as a result, flow stress decreases with increment in temperature.

3.3 Calculation of Activation Energy

The flow stress, temperature and strain rate can be correlated by Arrhenius-type equations as follows [26]:

$$\dot{\epsilon} = A_1 \sigma^{n_1} \exp(-Q/RT) \quad (\text{For low stress}) \tag{5}$$

$$\dot{\epsilon} = A_2 \exp(\beta\sigma) \exp(-Q/RT) \quad (\text{For high stress}) \tag{6}$$

where σ is the flow stress; $\dot{\epsilon}$ is the strain rate; A_1, A_2, n_1 and β are material constants; T is the absolute temperature in Kelvin; R is the universal gas constant (8.314 J/mol/K); and Q is the activation energy of hot deformation (kJ/mol). A hyperbolic sine-type equation that is applicable for the entire stress level can be expressed as:

$$\dot{\epsilon} = A \sinh[h(\alpha\sigma)]^n \exp(-Q/RT) \tag{7}$$

where A , n are material constants and α is known as stress multiplier that is expressed as $\alpha = \beta/n_1 \text{ MPa}^{-1}$. The combined effect of the temperature and strain rate is expressed by a temperature-compensated strain rate parameter, namely the Zener–Hollomon parameter Z , which is given as:

$$Z = \dot{\epsilon} \exp(Q/RT) \quad (8)$$

By combining Eqs. (7) and (8), a new equation can be expressed as follows:

$$Z = A[\sinh(\alpha\sigma)]^n \quad (9)$$

In this study, the peak stress under various conditions is taken into consideration for further calculation. Applying natural logarithm on both sides of Eqs. (5) and (6), the following equations are obtained:

$$\ln \dot{\epsilon} = \ln A_1 + n_1 \ln \sigma - (Q/RT) \quad (10)$$

$$\ln \dot{\epsilon} = \ln A_2 + \beta \sigma - (Q/RT) \quad (11)$$

The relationships between $\ln \sigma$ and $\ln \dot{\epsilon}$ and between σ and $\ln \dot{\epsilon}$ are displayed in Fig. 3a, b, respectively. Linear fitting of the curves provides the values of slopes which are eventually the values of n_1 and β at different temperatures, respectively. The average values of n_1 and β are deduced as 17.2507 and 0.1210, respectively. The value of the material constant α is calculated as 0.0070 MPa^{-1} .

Natural logarithm on both sides of Eq. (7) gives the following equation:

$$\ln \dot{\epsilon} = \ln A + n \ln[\sinh(\alpha\sigma)] - (Q/RT) \quad (12)$$

Differentiation of Eq. (12) with respect to $1/T$ at a constant strain rate provides the subsequent relation:

$$Q = R \times n \times \left[\frac{d\{\ln \sinh[\alpha\sigma]\}}{d(1/T)} \right]_{\dot{\epsilon}} \quad (13)$$

The plots of $\ln[\sinh(\alpha\sigma)]$ versus $\ln \dot{\epsilon}$ and $1000/T$ versus $\ln[\sinh(\alpha\sigma)]$ are illustrated in Fig. 3c, d, respectively. The slopes of these two curves after fitting provide the values of n and $\left[\frac{d\{\ln \sinh[\alpha\sigma]\}}{d(1/T)} \right]_{\dot{\epsilon}}$ for different compression conditions. From the values of $\left[\frac{d\{\ln \sinh[\alpha\sigma]\}}{d(1/T)} \right]_{\dot{\epsilon}}$ slopes, activation energies at various temperatures and strain rates are calculated and represented in Table 2. The average activation energy is also calculated.

Logarithm on both sides of Eq. (9) transforms the equation as,

$$\ln Z = \ln A + n \ln[\sinh(\alpha\sigma)] \quad (14)$$

Linear fitting of the plot between $\ln[\sinh(\alpha\sigma)]$ and $\ln Z$ as shown in Fig. 3e gives the values of $\ln A$ (intercept) and n (slope) as 38.0723 and 11.5776, respectively.

It can be seen that activation energy decreases with an increase in temperature or strain rate and vice versa. The

activation energy or the movement of dislocations is very much dependent on the deformation temperature and how easily the minimum shear stress for deformation along the slip plane (Peierls–Nabarro) is overcome. The mobility of dislocations is enhanced with the increment in thermal energy. As the temperature rises up, new slip systems are activated and the dislocation movement by cross-slip and climb occurs without any difficulty which results in the decrement in activation energy. Now the effect of strain rate can be described as follows. When the strain rate is low, the rate of application of external load is also less. At this condition, the movement of dislocations is solely dependent on the thermal energy. Moreover, for a given dislocation density, the velocity of dislocations in a field of obstacles is proportional to strain rate. This refers to greater difficulty of dislocations flow at lower strain rate [17]. Thus, the activation energy at a lower strain rate is greater for a particular temperature. The effect of increment in strain rate on dislocation movement can be subdivided into three ways. Firstly, as the strain rate increases, the externally applied force also increases and this additional resolved shear force at the direction of dislocation movement reduces the requirement of thermal energy. Thus, the activation energy reduces at higher strain rate. Secondly, the multiplication rate of dislocations increases with increment in strain rate, which results in an increase in the probability of dynamic restoration and eases further movement of dislocations. Thirdly, greater entanglement between dislocations occurs at a higher strain rate and overall progress of dislocations diminishes. Here, in this case, the cumulative effect of the first two phenomena dominates the latter and it is reflected in experimental results. A similar type of trend has been seen and discussed in previous studies [17, 34, 35]. At a temperature of 773 K and a strain rate range of $0.1\text{--}10 \text{ s}^{-1}$, the activation energy is approximately in the range of grain boundary diffusion energy of pure aluminum ($\sim 84 \text{ kJ/mol}$) [29]; thus, the corresponding deformation mechanism may be grain boundary diffusion with controlled dislocation climb. At 673 K and strain rate $1\text{--}10 \text{ s}^{-1}$, the Q value is close to lattice self-diffusion energy of pure aluminum (142 kJ/mol). At 773 K and 0.01 s^{-1} , the Q value is higher than the grain boundary diffusion but lower than lattice self-diffusion. So the deformation may be controlled by dislocation climb [20]. At a comparatively lower temperature ($473/573 \text{ K}$), the values of Q are very high. That may be due to the presence of intermetallic particles obstructing the dislocation motion and providing solute drag effect at a comparatively lower temperature [36]. Earlier, the average activation energy of aluminum 5083 alloy has been reported in the range of $162\text{--}186 \text{ kJ/mol}$ [8–10], which is lower than the current overall value of activation energy. It is quite evident that the activation energy is dependent on

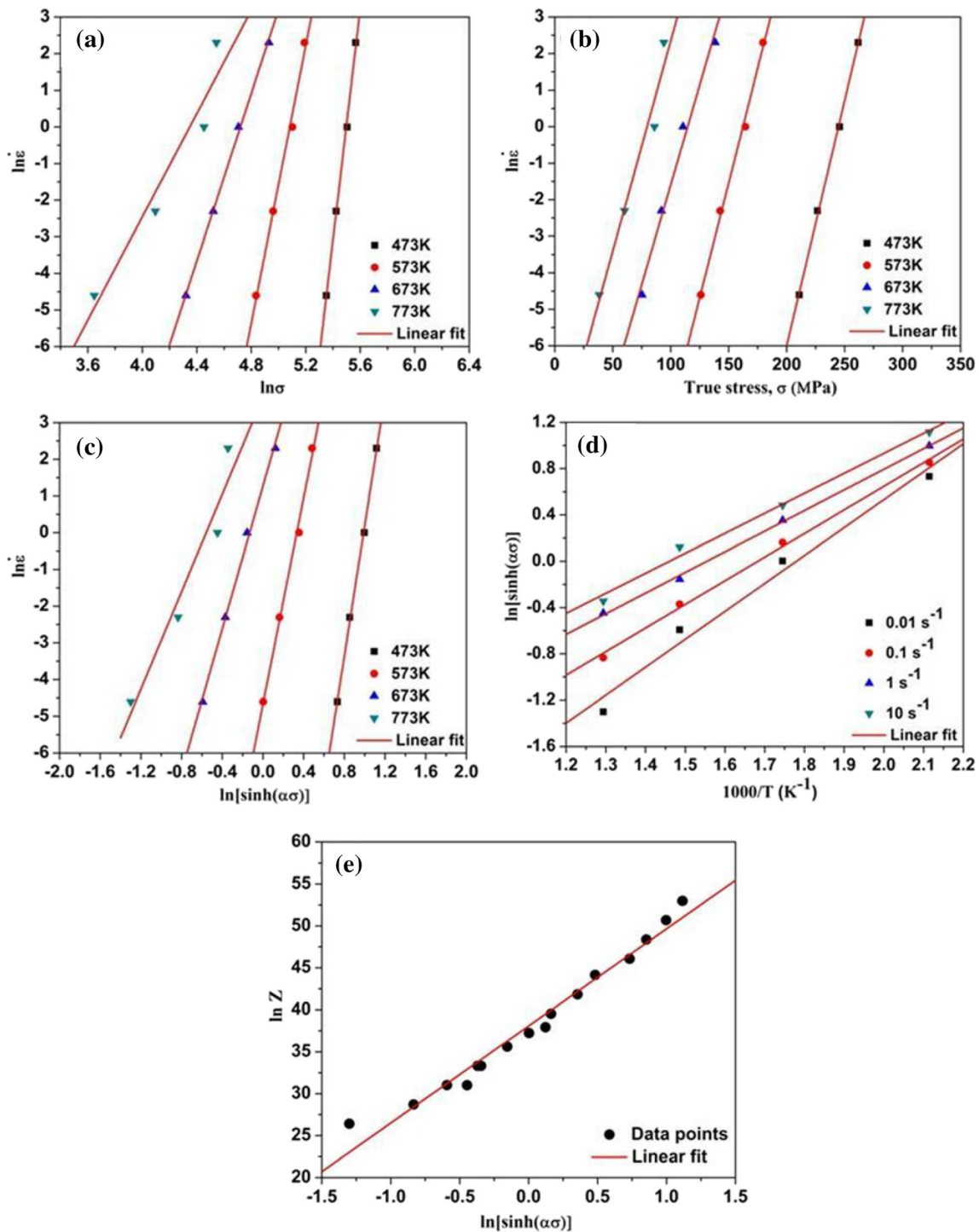


Fig. 3 Relationships between **a** $\ln \sigma$ and $\ln \dot{\epsilon}$; **b** σ and $\ln \dot{\epsilon}$, **c** $\ln \sinh(\alpha\sigma)$ and $\ln \dot{\epsilon}$, **d** $1000/T$ and $\ln \sinh(\alpha\sigma)$, **e** $\ln \sinh(\alpha\sigma)$ and $\ln Z$ for alloy

temperature and strain rate conditions, deformation state, alloy composition and grain structure. Thus, the change with previous values is very normal.

3.4 Processing Map

3.4.1 Establishment of Processing Map

To calculate the efficiency (η) and instability parameter (ζ), the relationship between $\ln \sigma$ and $\ln \dot{\epsilon}$ at a given strain and

Table 2 Values of activation energy (Q in KJ/mol) for alloy and composites at different temperature and strain rate

Materials	Strain rate (s^{-1})	Activation energy in KJ/mol			
		473 K	573 K	673 K	773 K
Alloy	0.01	356.2501	281.5657	195.1325	133.0703
	0.1	301.3282	238.1576	165.0495	112.5553
	1	263.2921	208.0954	144.2156	98.34769
	10	255.1674	201.6741	139.7654	95.31288
	Average activation energy	294.0095	232.3732	161.0408	109.8216
	Overall activation energy	199.3112			

temperature can be represented as a third-order polynomial equation as shown below [18]:

$$\ln \sigma = a + b \ln \dot{\epsilon} + c(\ln \dot{\epsilon})^2 + d(\ln \dot{\epsilon})^3 \quad (15)$$

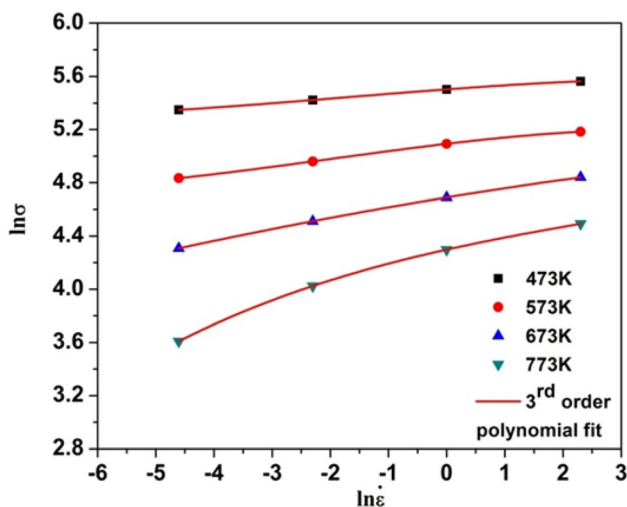
where a , b , c , d are the material constants. Now strain rate sensitivity m can be defined as follows:

$$m = \left[\frac{\partial(\ln \sigma)}{\partial(\ln \dot{\epsilon})} \right]_{\epsilon, T} = b + 2c \ln \dot{\epsilon} + 3d(\ln \dot{\epsilon})^2 \quad (16)$$

Now the third-order polynomial fittings of the curve between $\ln \sigma$ and $\ln \dot{\epsilon}$ give the required material constant values for evaluating m at a different temperature as shown in Fig. 4. The flow stress values at the final stage, i.e., true strain 0.5, have been considered to calculate m .

From the calculated values of m , the efficiency parameter η and the instability parameter ζ are evaluated according to the following equations [17]:

$$\eta = J/J_{\max} = \frac{2m}{m+1} \quad (17)$$

**Fig. 4** Logarithmic variations of σ as a function of strain rate for alloy

$$\zeta(\dot{\epsilon}) = \frac{\partial \ln(m/m+1)}{\partial \ln \dot{\epsilon}} + m < 0 \quad (18)$$

After obtaining the power dissipation map and instability map at a true strain of 0.5, the corresponding processing map is obtained by superimposing both of them as shown in Fig. 5. In the processing map, there is one shaded region at a temperature range of 473–663 K and strain rate from 0.4 to 10 s^{-1} , which represents the occurrence of instabilities during processing. It can also be observed that as the temperature increases, the power dissipation efficiency also increases. The highest power dissipation efficiency for the present alloy is obtained at 773 K and 0.01 s^{-1} where nearly 36% of energy has been utilized in microstructural formations. This is also the optimum condition for processing under the current scenario according to the processing map. Figure 6 represents the change in efficiency and instability area with respect to variation in strain from 0.2 to 0.5. As the strain increases, the area under the instability region increases and so is the percentage of efficiency. This also gives a better insight into the influence of temperature, strain rate and strain altogether. Now dynamic recrystallization or recovery is a process controlled by dislocation movement. The dislocation cross-slip, glide and mainly climb get accelerated tremendously with an increase in temperature. It takes time to accumulate the critical dislocation density to trigger the dynamic recrystallization, and the more is the time and temperature, the more and easier will be the grain boundary migration [37]. This may be the reason for obtaining the highest efficiency at the highest temperature and lowest strain rate condition compared to others.

3.4.2 Microstructural Study

The EBSD micrographs of the alloy samples undergoing different processing conditions are represented in Fig. 7. Both the image quality (IQ) map and inverse pole

Fig. 5 Processing map of alloy at a true strain of 0.5

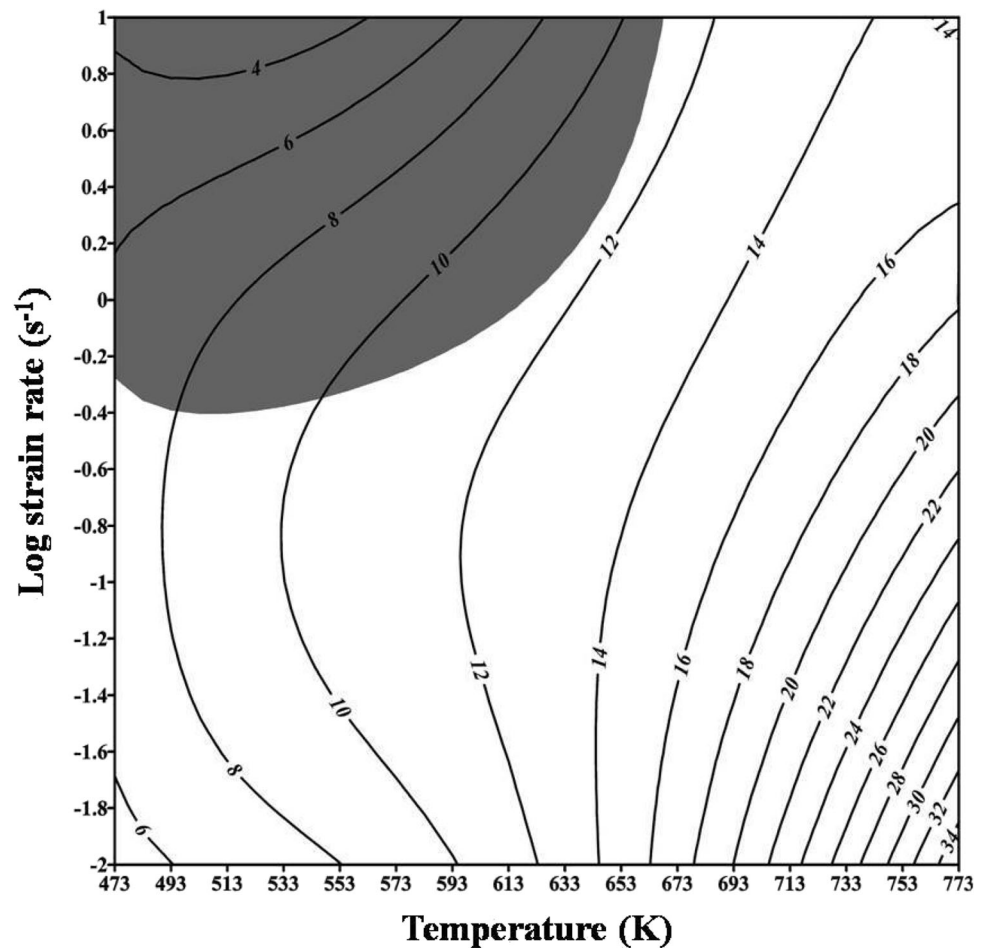


figure (IPF) map are shown for better representation. The IQ and IPF maps of the deformed specimen at 773 K and 0.01 s^{-1} are shown in Fig. 7a. The occurrence of subgrains formed by low-angle grain boundaries (2° – 15°) within the elongated grains can be clearly seen. This is a typical structure of dynamic recovery (DRV). In addition to this, new recrystallized grains are formed at the original grain boundaries as it is the place where large pinning of dislocations occurs. Thus, a necklace type of structure is created which is a clear indication of discontinuous dynamic recrystallization (DDRX). During deformation, dislocations are largely pinned at local serrations of original grain boundaries and result in bulging. It is followed by strain-induced boundary migration and local lattice rotation, which are ultimately responsible for the occurrence of dynamically recrystallized grains [29]. Along with the recrystallized grains at the parent grain boundaries, few recrystallized grains are also observed next to the second-phase particles (appeared as black in the EBSD image). As concluded from the earlier literature, the presence of second-phase particles greater than $1 \mu\text{m}$ nucleates new grains and stimulates the recrystallization process. However,

particles of submicron size ($< 1 \mu\text{m}$) pin the grain boundary migration and retard recrystallization [29, 36]. Due to the large orientation difference with respect to the primary phase, these large particles ($> 1 \mu\text{m}$) pin the dislocations and as a result, cell structures are formed next to them. Then, after reaching a critical strain, these cells coalesce and a nucleation of new grains occurs. This is also termed as particle-stimulated nucleation (PSN). In the present case, the observed second-phase particles are intermetallic compounds of Al–Mg and Al–Mg with Mn/Fe/Si as shown in EDX results and a size of these particles is much greater than $1 \mu\text{m}$. These large second-phase particles promote the PSN mechanism and take part in the recrystallization during deformation. It can be also observed that the growth of these new PSN grains is restricted by other recrystallized grains in the surrounding as shown in the EBSD image at higher magnification. A similar kind of recrystallized grains formed by PSN has been reported in the case of Al-5083 alloy by previous studies [38, 39]. In Fig. 7b, c, the IQ and IPF maps of samples deformed at temperature 773 K with a strain rate of 0.1 s^{-1} and 1 s^{-1} are shown, respectively. The

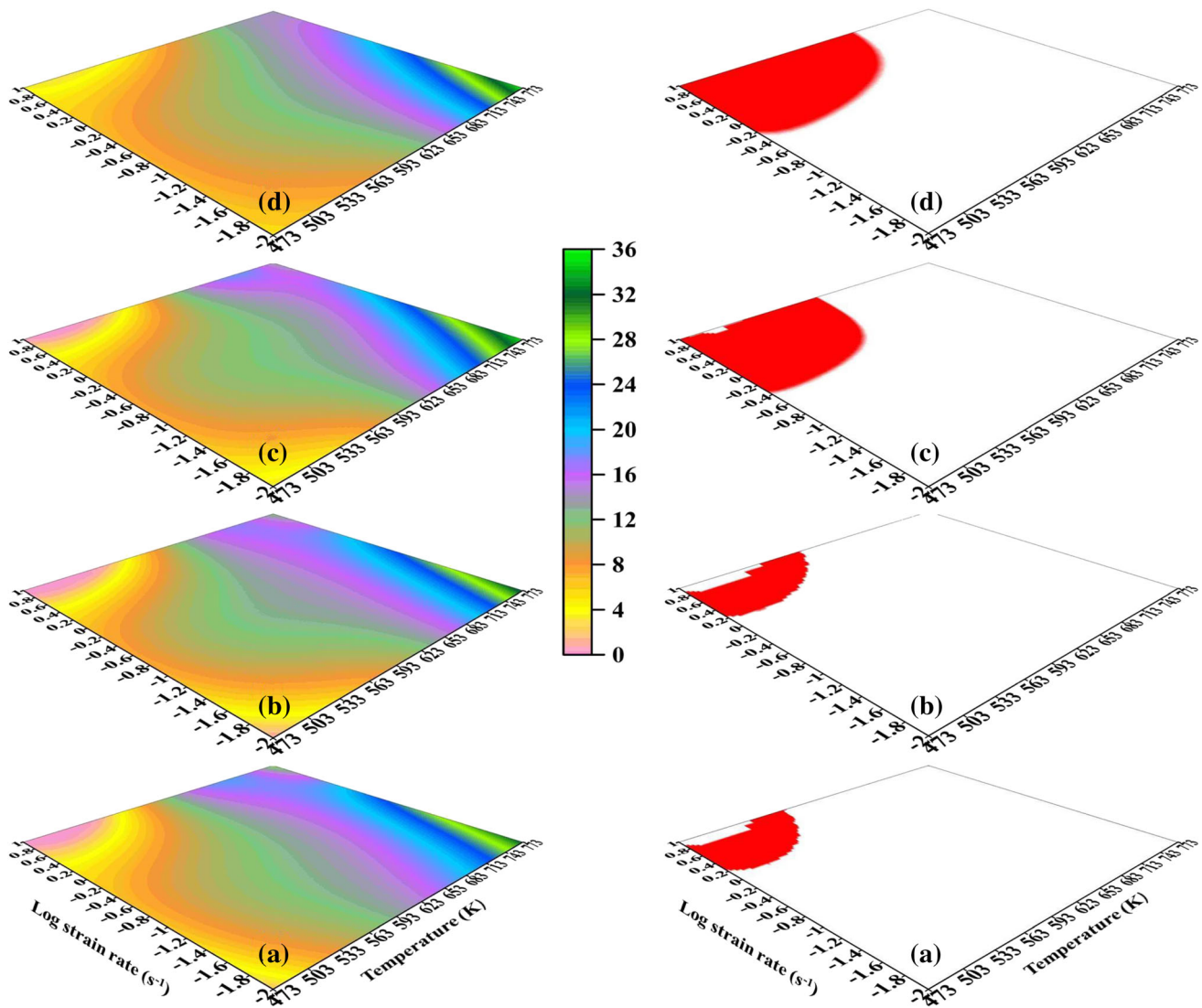


Fig. 6 Power dissipation efficiency map (left) and instability map (right) of al-5083 alloy at true strain **a** 0.2, **b** 0.3, **c** 0.4 and **d** 0.5. [The color scale shows the efficiency percentages]

deformation at this condition also reveals the coexistence of dynamic recovery and dynamic recrystallization mechanism in the material. It can be easily seen that at a temperature of 773 K, as the strain rate increases from 0.01 to 1 s^{-1} , the fraction of DRX grains decreases steadily. This is because there is little time available at higher strain rate for DRX to occur as nucleation and grain boundary migration are time-dependent phenomena. Figure 7d represents the IQ map and IPF map of the deformed specimen at 673 K and 0.01 s^{-1} , respectively. Here also, low-angle grain boundaries or subgrains (gray lines in IQ map) are formed within the elongated grains to accommodate the deformation with fewer evidence of DRX grains compared to the condition of 773 K/ 0.01 s^{-1} . As the temperature is comparatively low, the occurrence of DRX phenomenon also diminishes.

The misorientation angle distribution in Fig. 8 reveals the fraction of high-angle grain boundary (HAGB) ($> 15^\circ$) and low-angle grain boundary (LAGB) ($< 15^\circ$), which supports the microstructure as described. The occurrence of HAGBs is highest at 773/ 0.01 s^{-1} where DRX is most favorable. The pattern of the fraction of recrystallized grains is reflected in processing map as shown in Fig. 5 where the maximum efficiency occurs at 773 K/ 0.01 s^{-1} .

Figure 9a–c shows different microstructural features at different deformation conditions corresponding to the instability region in the processing map. At a comparatively lower temperature (473 K and 573 K) and a high strain rate (10 s^{-1}), flow localization in the form of interfacial cracking and grain boundary cracking is seen as shown in Fig. 9a, b. Similar kinds of microstructural phenomena were observed in aluminum 5xxx series alloys by

Fig. 7 IQ and IPF maps of alloy at deformation condition: **a** 773 K and 0.01 s^{-1} with a magnified image of recrystallized grains (inset), **b** 773 K and 0.1 s^{-1} , **c** 773 K and 1 s^{-1} , **d** 673 K and 0.01 s^{-1}

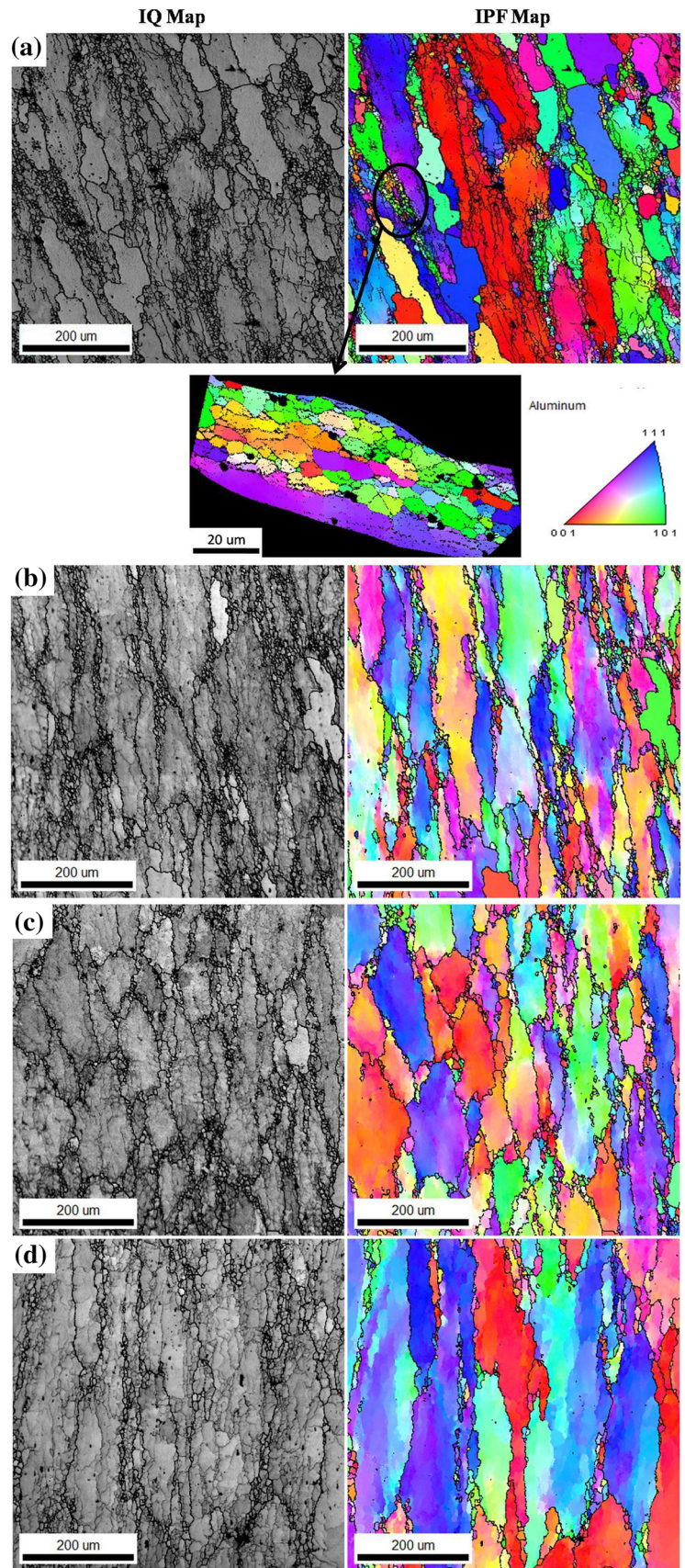


Fig. 8 Grain boundary misorientation distribution at deformation condition: **a** 773 K and 0.01 s^{-1} , **b** 773 K and 0.1 s^{-1} , **c** 773 K and 1 s^{-1} , **d** 673 K and 0.01 s^{-1}

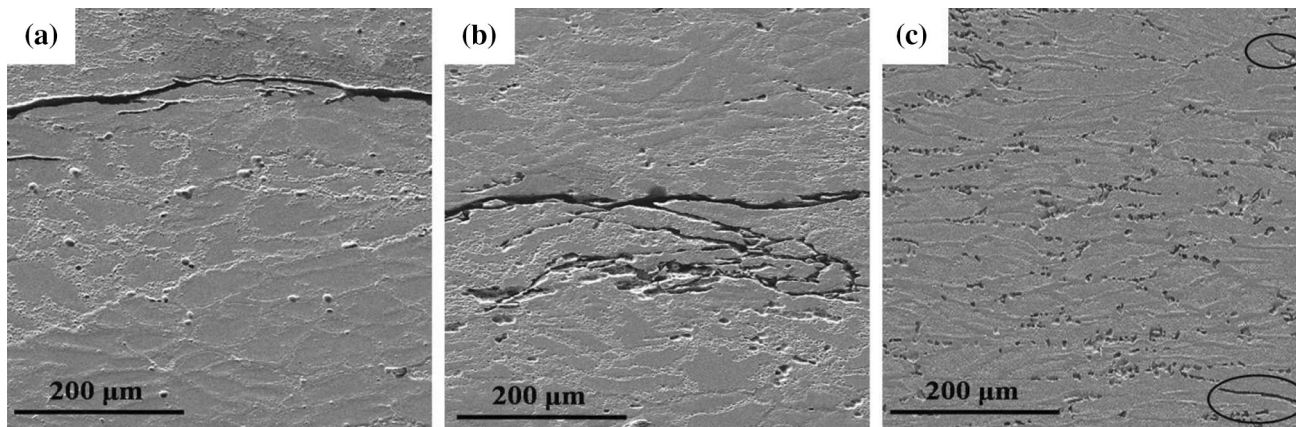
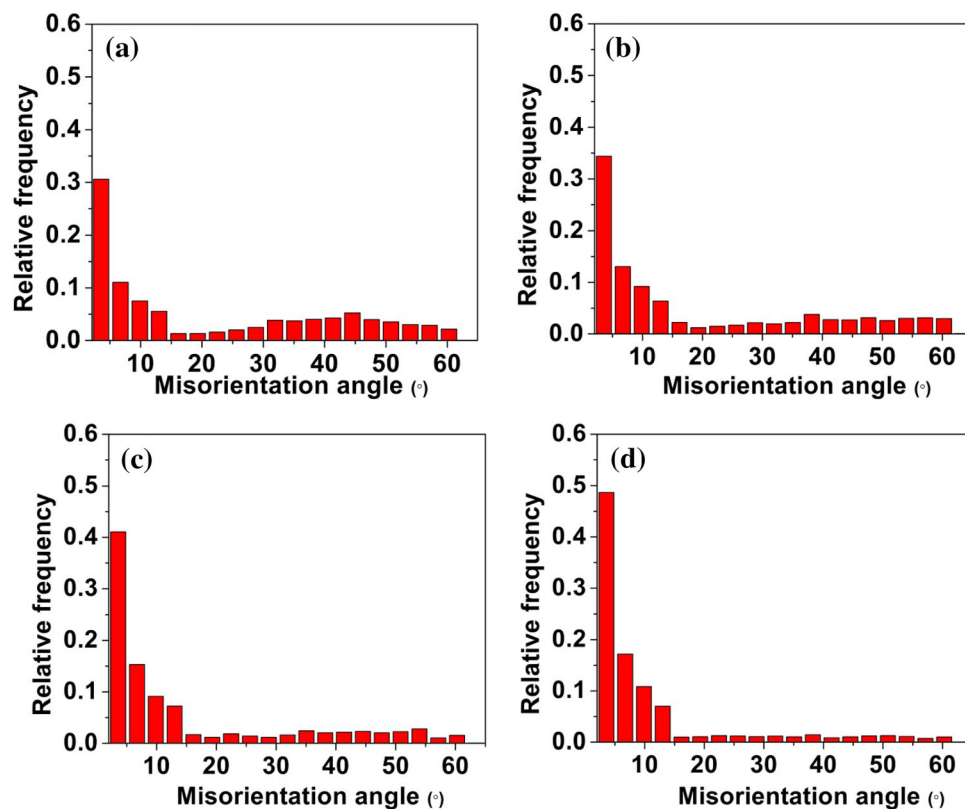


Fig. 9 **a** Severe interfacial cracking and grain boundary cracking due to intense flow localization at deformation condition 473 K and 10 s^{-1} , **b** Similar interfacial cracking at deformation condition 573 K and 10 s^{-1} , **c** Intercrystalline cracking at deformation condition 673 K and 10 s^{-1}

previous researchers [40]. At a high temperature and a high strain rate, formation of low temperature melting compounds due to local segregation of alloying elements can occur which is followed by their localized melting. This may cause creation and propagation of cracks along the grain boundaries [37]. This is also known as intercrystalline cracking and has been observed at deformation condition of 673 K and 10 s^{-1} as shown by marked regions in Fig. 9c. This processing condition almost coincides with the shaded instability region; hence, it should be avoided.

So, the processing map and corresponding microstructural examinations at various deformation conditions suggest that the optimum hot working parameter is 773 K and 0.01 s^{-1} is the highest percentage of DRX grains that has occurred there. However, the deformation condition of 673 K to 773 K and 0.01 s^{-1} to 2.5 s^{-1} gives a fair chance of hot processing.

3.5 Hot Rolling

3.5.1 Rolling Schedule

The details of the work plans that are followed during the hot rolling process are presented in Table 3. Seven specimens have been chosen and leveled as per their serial number. Each specimen has been planned to undergo different percentages of rolling reductions starting from 20% to 80% of the initial thickness. It can be seen that the odd-numbered specimens such as 1, 3, 5 and 7 have undergone 20%, 40%, 60% and 80% thickness reductions,

respectively, whereas even-numbered specimens such as 2, 4 and 6 have undergone 30%, 50% and 80% thickness reductions, respectively. The homogenized specimens are heated at a temperature of 793 K to account for some heat loss before rolling for 20 min at a furnace adjacent to the rolling mill to obtain temperature homogeneity. During rolling, the velocity of rolls is maintained at 2 m/min or 33.33 mm/s. The radius of the roll is 82.5 mm. The rollers are heated up to 623 K and maintained at that temperature throughout the rolling process in order to prevent a sudden drop in specimen temperature. The delay time is on an average 2 s between withdrawals from the furnace and

Table 3 Work plan and calculation of mean strain rate during hot rolling

Serial number of samples	1	2	3	4	5	6	7
Reduction percentage	20	30	40	50	60	70	80
Initial thickness (mm)	8	8	8	8	8	8	8
Mean strain rate(s ⁻¹)(L)/ Strain(R)	0.6473 ↓ 0.2231	0.8448 ↓ 0.3567	0.6473 ↓ 0.2231	0.8448 ↓ 0.3567	0.6473 ↓ 0.2231	0.8448 ↓ 0.3567	0.6473 ↓ 0.2231
Thickness after 1 st pass (mm)	6.4 (W.Q)	5.6 (W.Q)	6.4 (I.A)	5.6 (I.A)	6.4 (I.A)	5.6 (I.A)	6.4 (I.A)
Mean strain rate(s ⁻¹)(L)/ Strain(R)			0.8346 ↓ 0.2877	0.9761 ↓ 0.3365	0.8346 ↓ 0.2877	0.9761 ↓ 0.3365	0.8346 ↓ 0.2877
Thickness after 2 nd pass (mm)			4.8 (W.Q)	4.0 (W.Q)	4.8 (I.A)	4.0 (I.A)	4.8 (I.A)
Mean strain rate(s ⁻¹)(L)/ Strain(R)					1.1763 ↓ 0.4055	1.4819 ↓ 0.5108	1.1763 ↓ 0.4055
Thickness after 3 rd pass (mm)					3.2 (W.Q)	2.4 (W.Q)	3.2 (I.A)
Mean strain rate(s ⁻¹)(L)/ Strain(R)							2.0108 ↓ 0.6931
Thickness after 4 th pass (mm)							1.6 (W.Q)

I.A = Intermediate Annealing, W.Q = Water Quenching, L/R = Left/Right.

I.A, intermediate annealing; W.Q, water quenching; L/R, left/right

placing between the rolls. The specimen which has undergone higher percentage reduction ($> 30\%$ of initial thickness) is further placed in the furnace at the end of each cycle for 5 min (at 793 K) for intermediate annealing. When the required percentage reduction of initial thickness is achieved for a specimen, it undergoes immediate water quenching.

During hot rolling, the occurrence of sticking friction can be assumed between the specimen surface and roller. As for sticking friction, the relation between mean strain rate and rolling parameters is given as [41],

$$\bar{\dot{\epsilon}} = V_r \sqrt{\frac{1}{R(h_i - h_f)}} \ln \frac{h_i}{h_f} \quad (19)$$

where $\bar{\dot{\epsilon}}$ is the mean strain rate, V_r is the linear velocity of the rolls in mm/s, R is the radius of the rolls in mm, h_i is the initial thickness of the strip/plate, h_f is the final thickness of the strip/plate. The mean strain rate and the true compressive strain between each of the passes are calculated and shown on the left side and right side of the arrow mark in Table 3, respectively. From the processing maps at different strains as shown in Fig. 7, it can be said that the rolling process has been done within the safe zone criteria for processing. Though the true compressive strain involved during 80% reduction is slightly higher (0.69) than the current experimental condition of hot compression (0.5), no failure is observed during the corresponding rolling. The final conditions of strips after hot rolling are displayed in Fig. 10. It can be seen that rolling has been successfully executed avoiding any major crack formation or defects.

3.5.2 Microstructural Study

In Fig. 11, the EBSD micrographs of alloy samples undergoing different rolling reductions are shown. After a 20% reduction in initial thickness, there is very little change in grain dimensions as shown in Fig. 11a. Some



Fig. 10 Rolled plates of alloy up to 80% reduction in initial thickness

recrystallized grains are formed adjacent to the intermetallic particles (nonindexed points). It may be because the dislocation density close to intermetallics is comparatively higher than the original grain boundary at low deformation strain (20% reduction) that leads to DRX adjacent to intermetallics only rather than at boundary. After a 40% reduction, the grains are more elongated along the rolling direction and the original large grains contain subgrains within it as shown in Fig. 11b. It can also be seen that more number of DRX grains is formed near the second-phase particles and some are formed at original grain boundaries. The recrystallized grains are also elongated, which contain subgrains and have serrated grain boundaries, which indicates that they are recrystallized dynamically as shown in higher magnification image of 40% reduction. At 60% reduction in initial thickness, the fraction of recrystallized grains increases and their average size decreases compared to the previous pass (40% reduction) as shown in Fig. 11c. This may be due to the fact that the amount of deformation strain and strain rate involved are higher than the previous pass, respectively. Figure 11d reveals the deformation microstructure of alloy after 80% reduction in initial thickness. It is observed that DRX grains are very small due to involvement of high strain rate ($\sim 2 \text{ s}^{-1}$). It is worthy to mention here that despite the involvement of higher compressive strain than the previous pass, the recrystallized fraction does not change much. The reason may be lesser time available for nucleation of new grains due to high strain rate. This is also evident from processing map that for a particular strain and temperature, the power dissipation efficiency decreases with increase in strain rate (Fig. 5). It is also evident from misorientation angle distribution graph (Fig. 12a–d) that shows the fraction of HAGB is quite low at 20% reduction, which eventually reduces continuously at the expense of LAGB with an increment in rolling reduction.

Previous researches on hot rolling and annealing of Al 5083 and other aluminum alloy reveal some interesting facts which can be correlated here. The occurrence of static recrystallization (SRX) during annealing after hot deformation depends mainly on deformation temperature, initial grain size, deformation strain and annealing temperature and time. The observation suggests a few points. The amount of stored energy after deformation at around 773 K of this high-recovery-prone alloy is too less to promote SRX during annealing. The large initial grain size retards nucleation during annealing. The involvement of small amount of strain during deformation at each pass also retards the occurrence of SRX [14, 29, 42]. Consideration of these factors along with the fact that a short annealing time (300 s) is involved in the present case suggests very less chance of SRX though there is always the chance of grain growth of DRX grains during intermediate annealing.

Fig. 11 IQ and IPF map of alloy after rolling reduction of **a** 20%, **b** 40% with magnified image of recrystallized grains (inset), **c** 60%, and **d** 80%

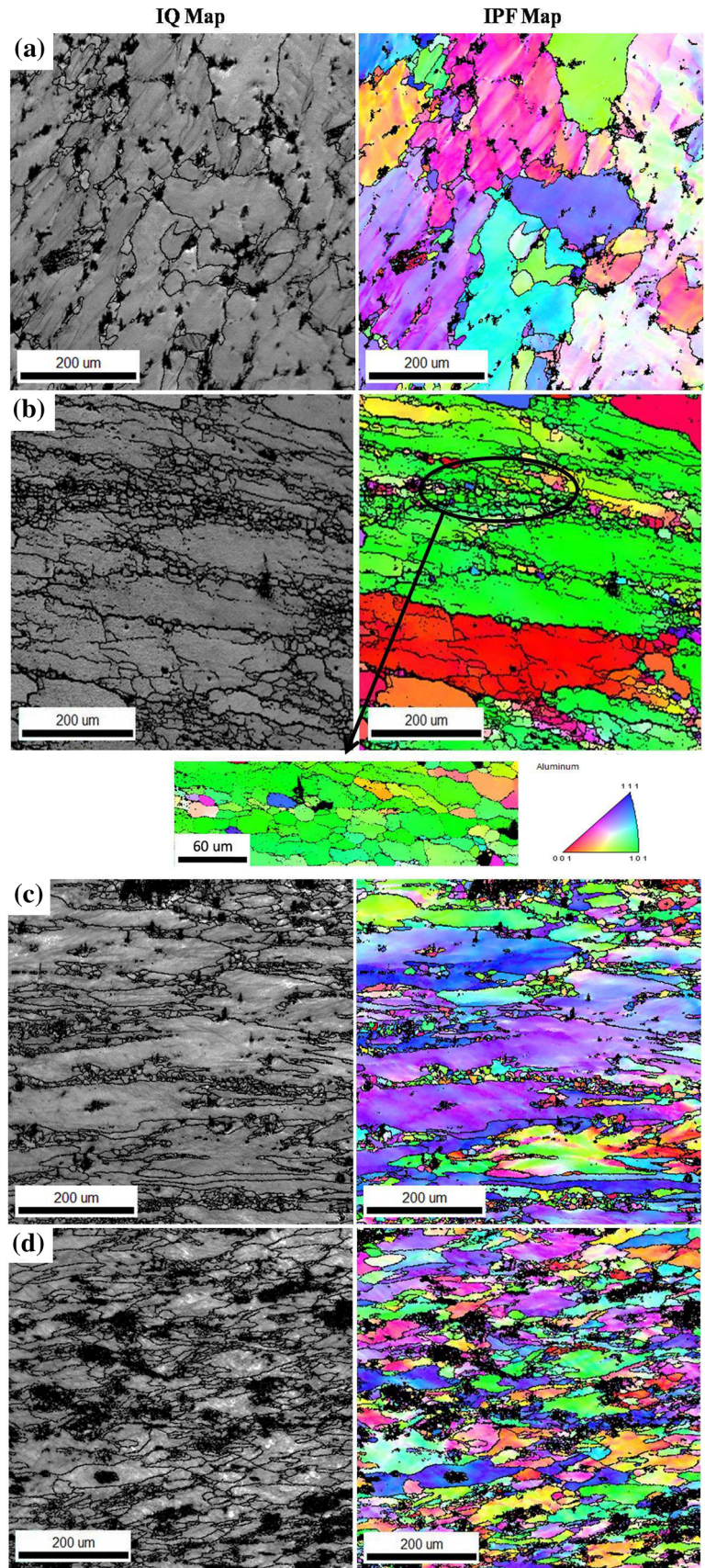
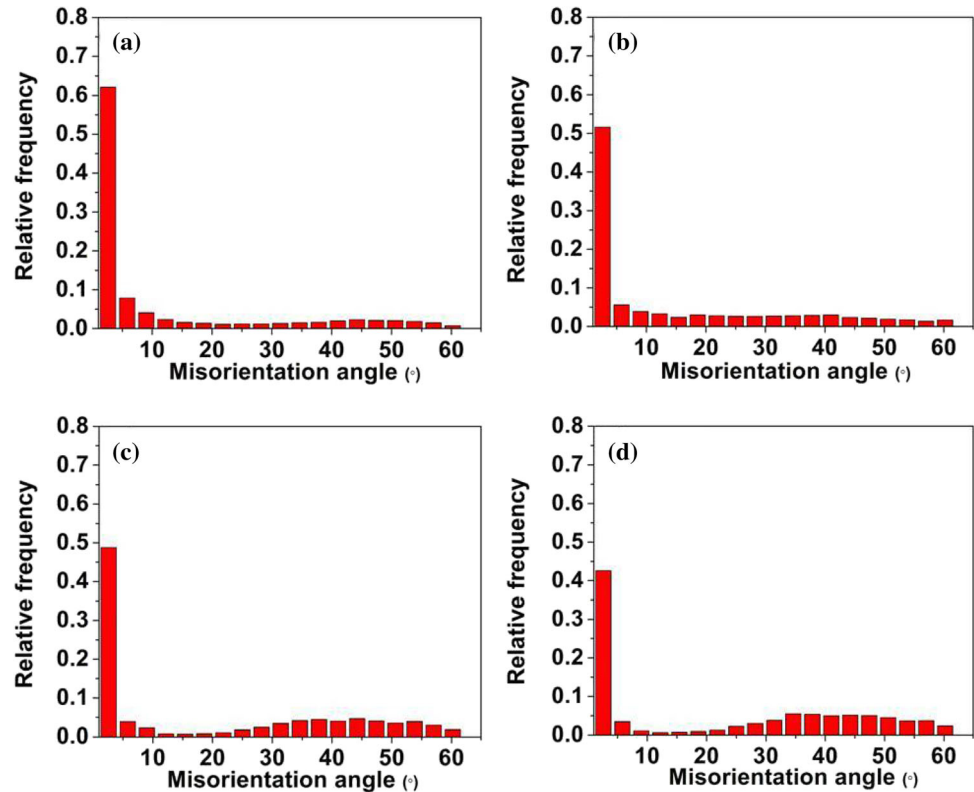


Fig. 12 Grain boundary misorientation distribution after rolling reduction of **a** 20%, **b** 40%, **c** 60%, and **d** 80%



3.5.3 Tensile and Bulk Hardness Testing

The room-temperature tensile test results of alloy in as-cast condition and different rolled conditions are represented in Fig. 13 as well as in Table 4. It can be seen that there is little increment in strength after a 20% reduction compared to as-cast condition. It may be due to limited grain refinement at this condition as shown before. With the increment in reduction, a marked increment in strength is

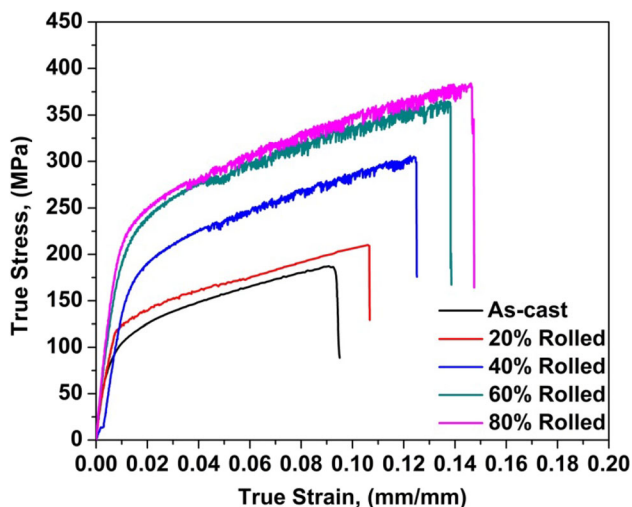


Fig. 13 Tensile test result in as-cast condition and different rolling conditions

also noticed. As the reduction increases, the fraction of recrystallized grains increases with a decrement in their average size. It is observed by previous studies that original grains get more elongated with an increment in reduction and formation and coalescence of subgrains occur within them [29]. Dislocations pinning at these recrystallized grain (DRX) boundaries and subgrain boundaries is the main reason for this increment in strength. Moreover, the elongation to fracture also increases with increment in reduction. The possible reason behind this may be the propagation of crack through the grain boundaries slows down as it turns out to be more difficult to go through the randomly oriented grains. This difficulty increases with the increment in the fraction of recrystallized grains and results in delay in complete fracture. It can be explained in other way that for a certain amount of second-phase particles, higher the number of high-angle grain boundary or DRX grains, fewer will be the distribution of those particles among them. This can prolong the fracture mechanism to progress as strain concentration at grain boundary will be comparatively less [43]. Previously, the room-temperature yield strength, ultimate tensile strength and elongation to fracture of monolithic Al-5083 alloy in extruded condition (at 753 K with extrusion ratio of 16:1) have been reported as 165 MPa, 320 MPa and 14.4%, respectively [44]. These values of tensile properties are comparable with 60% of reduced rolled samples in the present case. Another very

Table 4 Values of mechanical properties of alloy under different conditions

Material condition	Yield strength (MPa)	Ultimate tensile strength (MPa)	Total elongation (%)	Hardness (BHN)
As cast	83.15 ± 6.78	187.15 ± 8.97	9.59 ± 0.44	69.49 ± 2.14
20% rolled	112.48 ± 5.98	209.88 ± 10.47	11.19 ± 0.28	72.87 ± 2.81
40% rolled	144.84 ± 8.78	305.17 ± 11.78	13.18 ± 0.34	81.44 ± 2.86
60% rolled	172.95 ± 7.71	364.45 ± 11.48	14.69 ± 0.21	85.67 ± 3.45
80% rolled	191.05 ± 8.12	384.19 ± 12.47	15.74 ± 0.31	88.81 ± 2.95

important Al-5xxx series alloy Al-5052 has been cryorolled and cryo groove rolled to 90% reduction in initial thickness as reported in the literature [45]. These treatments imparts yield strength of 283 MPa and 304 MPa, respectively, while elongation to fracture has been reduced significantly to 6% and 3%, respectively, compared to the same mechanical properties as 160 MPa and 42% in solution-treated condition. However, annealing for 1 h at temperature 573 K helps to restore the elongation percentage to 9.6% and 8.25%, respectively, with final yield strength of 154 MPa and 228 MPa, respectively. Warm rolling at 448 K and annealing at 513 K of the same cryo groove rolled alloy have delivered an optimum combination of yield strength and elongation percentage of about 215 MPa and 15%, respectively [46]. These values are very much similar to mechanical properties of the current Al-5083 alloy after 80% reduction.

The same trend of the tensile test result is followed in Brinell hardness test as shown in Table 4. The dislocation motion during local plastic deformation is blocked by the subgrain boundaries as well as DRX grain boundaries. The difference in hardness between samples with 60% and 80% reduction is not that significant due to limited increment in the fraction of recrystallized grains as discussed earlier.

4 Conclusions

1. The activation energy for hot deformation of Al-5083 alloy under a vast processing condition (473–773 K/0.01–10 s⁻¹) was evaluated. The average activation energy was found to be 199.31 kJ/mol, which was higher than the previous reported values of activation energy of the same alloy. Consideration of larger processing range and homogenization of the material was the main reason for this increment.
2. The optimization of process parameters, prediction and validation of safe and unsafe zones for processing were successfully carried out by establishing processing map and subsequent microstructural study by EBSD and SEM analysis.

3. The safe zone was found to be in between 673 and 773 K and 0.01 s⁻¹ to 2.5 s⁻¹ with optimum processing parameter of 773 K and 0.01 s⁻¹. Dynamic recovery was the main softening mechanism at lower temperature (673 K), whereas dynamic recrystallization coexisted with dynamic recovery at a higher temperature (773 K). The temperature range of 473 K–663 K and strain rate from 0.4 to 10 s⁻¹ was detected as an unsafe zone as flow instabilities under this processing range were observed.
4. Hot rolling was attempted as per the safe zone conditions, and up to 80% reduction in initial thickness was achieved successfully. The rolling microstructure had the evidence of dynamic recrystallization, which increased with increment in percentage of reduction.
5. Significant and progressive increments in yield strength, ultimate tensile strength, ductility and hardness were achieved by hot rolling.

Acknowledgments The authors are grateful to the Director of CSIR-AMPRI, Bhopal, for providing the work facilities and consent for publishing this paper. The authors thank CSIR India (Grant No. 31/041/(0068)2015-EMR-I) and AcSIR-AMPRI, Bhopal, for providing fellowship and support, respectively.

Compliance with Ethical Standards

Conflict of interest The authors have no conflicts of interest to declare.

References

1. Tellkamp V, and Lavernia E, *Nanostruct. Mater.* **12** (1999) 249.
2. Kaibyshev R, Musin F, Lesuer D, and Nieh T, *Mater. Sci. Eng. A* **342** (2003) 169.
3. Summers P T, Mouritz A P, Case S W, and Lattimer B Y, *Mater. Sci. Eng. A* **632** (2015) 14.
4. Li J, Liu W, Zhai T, and Kenik E, *Scr. Mater.* **52** (2005) 163.
5. Xia S, Ma M, Zhang J, Wang W, and Liu W, *Mater. Sci. Eng. A* **609** (2014) 168.
6. Li J, Zeng Q, Wen X, and Zhai T, *Mater. Sci. Technol.* **23** (2007) 225.
7. Singh D, Rao P N, and Jayaganthan R, *Int. J. Miner. Metall. Mater.* **20** (2013) 759.

8. McQueen H, Evangelista E, Bowles J, and Crawford G, *Met. Sci.* **18** (1984) 395.
9. McQueen H, Fry E, and Belling J, *J. Mater. Eng. Perform.* **10** (2001) 164.
10. Fang G, Liao P-G, Zhou J, and Duszczyc J, *New Frontiers in Light Metals: Proceedings of the 11th International Aluminum Conference INALCO 2010*, IOS Press, 2010, p. 431.
11. Zhong W, Goiffon E, L'Espérance G, Suéry M, and Blandin J, *Mater. Sci. Eng. A* **214** (1996) 84.
12. Wells M, Maijer D, Jupp S, Lockhart G, and Van der Winden M, *Mater. Sci. Technol.* **19** (2003) 467.
13. Duan X, and Sheppard T, *Modell. Simul. Mater. Sci. Eng.* **10** (2002) 363.
14. Raghunathan N, Zaidi M, and Sheppard T, *Mater. Sci. Technol.* **2** (1986) 938.
15. Prasad Y, Rao K, *Mater. Sci. Eng. A* **391** (2005) 141.
16. Prasad Y, Seshacharyulu T, *Mater. Sci. Eng. A* **243** (1998) 82.
17. Wang S, Hou L, Luo J, Zhang J, and Zhuang L, *J. Mater. Process. Technol.* **225** (2015) 110.
18. Li H, Wang H, Liang X, Liu H, Liu Y, and Zhang X, *Mater. Sci. Eng. A*, **528** (2011) 1548.
19. Liu Y, Geng C, Lin Q, Xiao Y, Xu J, and Kang W, *J. Alloys Compd.* **713** (2017) 212.
20. Deng K-k, Li J-c, Xu F-j, Nie K-b, and Liang W, *Mater. Des.* **67** (2015) 72.
21. Yang Y, Zhang Z, and Zhang X, *Mater. Sci. Eng. A* **558** (2012) 112.
22. Senthilkumar V, Balaji A, and Narayanasamy R, *Mater. Des.* **37** (2012) 102.
23. Huang Z, Zhang X, Xiao B, and Ma Z, *J. Alloys Compd.* **722** (2017) 145.
24. Mokdad F, Chen D, Liu Z, Ni D, Xiao B, and Ma Z, *Mater. Sci. Eng. A* **702** (2017) 425.
25. Chen L, Zhao G, Yu J, and Zhang W, *Mater. Des.* (1980–2015), **66** (2015) 129.
26. Chen L, Zhao G, and Yu J, *Mater. Des.* **74** (2015) 25.
27. Aballe A, Bethencourt M, Botana F, Cano M, and Marcos M, *Corros. Sci.* **43** (2001) 1657.
28. Engler O, and Miller-Jupp S, *J. Alloys Compd.* **689** (2016) 998.
29. Humphreys F J, and Hatherly M, *Recrystallization and related annealing phenomena*, 2nd ed., Elsevier (2012).
30. Abbasi-Bani A, Zarei-Hanzaki A, Pishbin M, and Haghdadi N, *Mech. Mater.* **71** (2014) 52.
31. Shi C, Lai J, and Chen X, *Mater.* **7** (2014) 244.
32. Lin Y, Chen M-S, and Zhong J, *Mech. Res. Comm.* **35** (2008)142.
33. Wei W, Wei K, and Fan G, *Acta Mater.* **56** (2008) 4771.
34. Honeycombe, R W K, *The plastic deformation of metals*, Edward Arnold London (1968).
35. Shi C, Mao W, and Chen X-G, *Mater. Sci. Eng. A* **571** (2013) 83.
36. McQueen H J, Spigarelli S, Kassner M E, and Evangelista E, *Hot deformation and processing of aluminum alloys*, CRC Press (2016).
37. Prasad Y, and Seshacharyulu T, *Int. Mater. Rev.* **43** (1998) 243.
38. Humphreys F, *Acta Metall.* **25** (1977) 1323.
39. McQueen H, and Jonas J, *J. Appl. Metalworking* **3** (1984) 233.
40. Prasad Y, Rao K, and Sasidhar S, *Hot working guide: a compendium of processing maps*, 2nd ed., ASM International (2015).
41. Harris J N, *Mechanical working of metals: theory and practice*, Elsevier (2014), p. 144.
42. El-Sabbagh A, Soliman M, Taha M, and Palkowski H, *J. Mater. Process. Technol.* **212** (2012) 497.
43. Abolhasani A, Zarei-Hanzaki A, Abedi H, and Rokni M, *Mater. Des.* **34** (2012) 631.
44. Zhong W, Goiffon E, L'Espérance G, Suéry M, and Blandin J, *Mater. Sci. Eng. A* **214** (1996) 93.
45. Yogesha K, Kumar N, Joshi A, Jayaganthan R, and Nath S, *Metallogr. Microstruct. Anal.* **5** (2016) 251.
46. Yogesha K, Joshi A, Kumar N, and Jayaganthan R, *Mater. Manuf. Process.* **32** (2017) 1336.

Publisher's Note Springer Nature remains neutral with regard to jurisdictional claims in published maps and institutional affiliations.